

## Shell structure of the $A = 6$ ground states from three-body dynamics

D. R. Lehman and W. C. Parke

*Department of Physics, The George Washington University, Washington, D. C. 20052*

(Received 17 January 1983)

Three-body ( $\alpha NN$ ) models of the  ${}^6\text{He}$  and  ${}^6\text{Li}$  ground states are used to investigate their shell structure. Three models for each nucleus are considered: simple, full ( $nn$ ), and full ( $np$ ) for  ${}^6\text{He}$ , and simple, full (0%), and full (4%) for  ${}^6\text{Li}$ . The full models in both cases are obtained by including the  $S_{1/2}$ ,  $P_{1/2}$ , and  $P_{3/2}$  partial waves of the  $\alpha N$  interaction, whereas the simple model truncates to only the strongly resonant  $P_{3/2}$  wave. The  ${}^6\text{He}$  full models distinguish between use of the  $nn$  or  $np$  parameters for the  ${}^1S_0$   $NN$  interaction, while the  ${}^6\text{Li}$  full models have either a pure  ${}^3S_1$   $NN$  interaction (0%) or a  ${}^3S_1$ - ${}^3D_1$  interaction that leads to a 4%  $d$ -wave component in the deuteron (4%). These models are used to calculate the probabilities of the orbital components of the wave functions, the configuration-space single-particle orbital densities, and the configuration-space two-particle wave function amplitudes in  $j$ - $j$  coupling with the nucleon coordinates referred to the alpha particle as the "core" or "center of force." The results are then compared with those from phenomenological and realistic-interaction shell models. Major findings of the comparison are the following: None of the shell models considered have a distribution of orbital probabilities across shells like that predicted by three-body models; the orbital rms radii from three-body models indicate an ordering of the orbits within shells, i.e.,  $p_{1/2}$  outside  $p_{3/2}$ , unlike oscillator shell models with a single oscillator parameter where the  $p$ -shell orbitals have the same shape; and, as expected, three-body orbital densities decay at large radial distances as exponentials rather than the too compact Gaussian falling off of oscillator shell models.

[ NUCLEAR STRUCTURE  ${}^6\text{He}$  and  ${}^6\text{Li}$ , three-body models, shell structure. ]

### I. INTRODUCTION

Three-body models of the  $A=6$  system, that is, alpha particle plus two nucleons ( $\alpha NN$ ), with the dynamics actually solved as a three-body problem, provide the first fundamental picture of this system beyond standard approaches, e.g., shell models, that reduce in their effect to two-body dynamics. The significance of the three-body dynamics is apparent in our present understanding of elastic deuteron-alpha scattering, deuteron breakup on alpha particles, and the continuum states (resonances) of the  $A=6$  system.<sup>1,2</sup> The powerful content of such a treatment carries over as well to the structure of the  ${}^6\text{He}$  ( $0^+$ ) and  ${}^6\text{Li}$  ( $1^+$ ) ground states. The ground-state three-body binding energies are predicted to within 0.5 MeV, while the calculated energy difference between the  $J^\pi=0^+$  and  $1^+$  states of  ${}^6\text{Li}$  deviates from the experimental value by only a few percent.<sup>3-5</sup> The associated wave functions permit examination of other ground-state properties. So far, the alpha-deuteron structure of  ${}^6\text{Li}$  and the  ${}^6\text{He}$   $\beta$

decay have been considered. Specifically, the  ${}^6\text{Li} \rightarrow \alpha + d$  momentum distribution,  ${}^6\text{Li} \rightarrow \alpha + d$  asymptotic norms, and the percentage alpha-deuteron component have been calculated and found to be in agreement with the corresponding experimental quantities.<sup>6</sup> The compositeness of the deuteron in the three-body model permits a deeper understanding of when "effective" alpha-deuteron models are valid. On the other hand, the excellent agreement with experiment for the  ${}^6\text{He}$   $\beta$  decay rate serves as a test of the  ${}^6\text{He}$ - ${}^6\text{Li}$  wave-function overlap and indicates that it is well tuned in the three-body models.<sup>7</sup> Although many other  $A=6$  properties remain to be investigated—charge form factors, quadrupole moment of  ${}^6\text{Li}$ , etc., the results obtained so far indicate the viability of this approach.<sup>8</sup> Its strength lies in the origin of the model: The only input is the basic two-body interactions—nucleon-nucleon and alpha-nucleon. Moreover, the model is formulated in the center-of-mass system, thus eliminating the need for center-of-mass corrections in calculations as required in shell-model work.<sup>9</sup> For

TABLE I. Shell model wave-function-component amplitudes as defined in Eqs. (1) and (2).

Source	$A$	$B$	$C$	$D$	$E$	$b$ (fm)
DW (Ref. 10)	0.810	-0.581	0.084	0.80	0.60	2.03
BAH (Ref. 12)						
Saskatoon A	0.810	-0.581	0.0839	0.998	0.0482	
Saskatoon B	0.810	-0.581	0.0839	0.816	0.577	
Vergados (Ref. 15) <sup>a</sup>						
I(a)	0.799	-0.600	-0.025	0.978	0.206	1.95
(b)	0.737	-0.675	-0.015	0.958	0.283	
II(a)	0.743	-0.629	-0.027	0.969	0.205	
(b)	0.683	-0.691	-0.017	0.957	0.245	
III(a)	0.729	-0.619	-0.027	0.941	0.215	
(b)	0.672	-0.674	-0.021	0.929	0.254	

<sup>a</sup>The (a) and (b) after the Roman numerals distinguish the two different sets of single-particle energies used as input. The Roman numerals represent, respectively, I inert core, II core excitation ( $2p+3p-1h$ ), and III: core excitation ( $2p+3p-1h+4p-2h$ ).

these reasons, it is compelling to use the predictive capabilities of three-body models to examine the shell structure of the  $A=6$  ground states.

In the mid-seventies, renewed effort was put forth in an attempt to unravel the structure of  ${}^6\text{Li}$  within the context of shell models. The work was motivated by the excellent electromagnetic data that had become available, e.g., magnetic moment, charge and magnetic form factors, and the electromagnetic transition form factors. Also, the  $\beta$ -decay rate of  ${}^6\text{He}$  is accurately known. Processes involving the first  $0^+$  state of  ${}^6\text{Li}$  can be related directly to processes involving the ground state of  ${}^6\text{He}(0^+)$  by assuming they are members of the same isospin multiplet. This approach has been used to predict the semileptonic weak rates of  ${}^6\text{He}$   $\beta$  decay,  $\mu$  capture on  ${}^6\text{Li}$ , and leptonic production of neutrinos on  ${}^6\text{Li}$ . It has been extended to the reaction  ${}^6\text{Li}(\gamma, \pi^+){}^6\text{He}$  as well. In fact, it was a 60% disagreement between theory and experiment for the latter reaction, while reasonable agreement existed for electromagnetic processes and  ${}^6\text{He}$   $\beta$  decay, that spurred the recent interest in the structure of the  $A=6$  wave functions. Two approaches have been used in an attempt to delineate their structure: (1) phenomenological shell-model calculations; and (2) shell-model calculations with realistic interactions.

The phenomenological wave function approach was initiated by Donnelly and Walecka (DW).<sup>10</sup> They attempted a unified analysis of semileptonic weak and electromagnetic processes involving the  ${}^6\text{Li}$  ground state, the  ${}^6\text{Li}$   $0^+$  state, and the  ${}^6\text{He}$  ground state, since the conserved-vector-current theory implies that weak matrix elements coming from the vector current are identical to those mea-

sured in electron scattering. By concentrating on the  $A=6$   $J^\pi T=1^+0$  ground state of  ${}^6\text{Li}$  and the  $0^+1$  isomultiplet, DW had at their disposal accurate elastic and inelastic electron scattering data with momentum transfers up to  $\sim 2 \text{ fm}^{-1}$ . DW truncate the space of the valence particles to the  $1p$  shell and assume a harmonic oscillator basis with a *single* oscillator parameter:

$$\begin{aligned}
 |1^+0\rangle = & A |(1p_{3/2})^2; 1^+0\rangle \\
 & + B |(1p_{3/2}1p_{1/2}); 1^+0\rangle \\
 & + C |(1p_{1/2})^2; 1^+0\rangle
 \end{aligned} \quad (1)$$

and

$$|0^+1\rangle = D |(1p_{3/2})^2; 0^+1\rangle + E |(1p_{1/2})^2; 0^+1\rangle. \quad (2)$$

Therefore, there are six parameters with two normalization constraints. The normalization conditions plus the magnetic and quadrupole moments of  ${}^6\text{Li}$  eliminate four parameters. The remaining two parameters, one being the oscillator parameter  $b$  (see Table I), are fixed by fitting the elastic and inelastic magnetic form factors. The charge form factor is not used on the basis that it receives contributions from the core particles, whereas DW take the core to be inert. DW introduce single-nucleon and center-of-mass form factors in their analysis. The accurate wave function amplitudes obtained by DW are similar to those found in earlier two-particle shell-model calculations,<sup>11</sup> with a notable exception:  $E$  is larger than the value obtained in the simple shell model (see Table I). When the DW wave functions are used to predict the  ${}^6\text{He}$   $\beta$  decay rate,

reasonable agreement with experiment is obtained, but the calculated  $\mu$ -capture rate lies well below the large experimental error limit. Moreover, very poor agreement with the cross sections for the  ${}^6\text{Li}(\gamma, \pi^+){}^6\text{He}$  reaction is obtained.

In an attempt to reconcile the  ${}^6\text{Li}(\gamma, \pi^+){}^6\text{He}$  predictions, Bergstrom, Auer, and Hicks<sup>12</sup> (BAH) reexamined the phenomenological approach of DW. They concluded that the weakest link was the  $M1$ -electroexcitation form factor and remeasured it over sufficient momentum-transfer range to include the values associated with the photopion and  $\mu$ -capture processes, and extracted the  $M1$  radiative width. They used the  $M1$  width as a constraint on the  $0^+1$  wave function. With newly constructed phenomenological wave functions based on generalizing the  $1p$ -shell harmonic oscillator forms, BAH conclude that the  $1p$  harmonic oscillator basis is inadequate. This conclusion was reaffirmed by Cammarata and Donnelly (CD) in their critical review of the entire situation.<sup>13</sup> Additionally, CD point out that the new wave functions generated by BAH do not give satisfactory agreement for the  ${}^6\text{He}$   $\beta$  decay,  $\mu$ -capture rate, and the then available  ${}^6\text{Li}(\gamma, \pi^+){}^6\text{He}$  data. Since then, the threshold pion photoproduction has been remeasured to a quoted accuracy of 4%.<sup>14</sup> Nevertheless, a consistent picture of the electromagnetic data,  ${}^6\text{He}$   $\beta$  decay,  $\mu$  capture, and threshold  ${}^6\text{Li}(\gamma, \pi^+){}^6\text{He}$  does not seem to arise from the phenomenological wave functions.

In light of the results for the phenomenological wave functions, what is the structure of the  $A=6$  wave functions obtained from shell-model calculations with realistic interactions? Do they lead to reasonable predictions for the properties and processes of interest? Recent work in that direction is that of Vergados.<sup>15</sup>

Vergados derives shell-model wave functions for the  $A=6$  system from two-body-interaction matrix elements of Kuo and Lee,<sup>15</sup> which are a modified version of the Kuo-Brown matrix elements.<sup>16</sup> In addition, he considers two sets of single-particle energies as input: (1) the set usually used for nuclei with the  $1p$  shell almost full; (2) a set obtained by fitting the  $2^+0$  and  $3^+0$  states of  ${}^6\text{Li}$  with the Kuo-Lee matrix elements. The oscillator parameter used was close to that of DW. Compared to DW, the distinctive aspects of the wave functions are that the  $0^+1$  wave function is very different and the amplitude of the  $|(1p_{1/2})^2; 1^+0\rangle$  component is a small negative value. The  $0^+1$  wave function resembles more one of the BAH wave functions (called Saskatoon A). (See Table I where the various wave-function-component amplitudes have been tabulated.) The predicted energy difference between the  $1^+0$  and  $0^+1$  states is considerably less than experiment. The

${}^6\text{Li}$  magnetic moment,  $M1$   $0^+1$  to  $1^+0$  radiative width, and  $\mu$ -capture rate are in reasonable agreement with experiment, but the  ${}^6\text{Li}$  quadrupole moment is large with the wrong sign, the  $\beta$ -decay  $ft$  value is too small, and the  $\pi$ -capture rate too large. When Vergados includes core excitations in his calculations, the predicted energy difference between the  $1^+0$  and  $0^+1$  states becomes larger, but not large enough; the sign of the quadrupole moment changes, but the magnitude is still incorrect; and the  $\beta$ -decay  $ft$  value is still in disagreement with experiment except for one case. Clearly, just as for phenomenological wave functions, a unified description of the  $A=6$  properties and processes of interest is not possible with the best available shell-model wave functions obtained from realistic interactions.

The aim of this paper is to investigate the shell structure of the  $A=6$  ground states as it is predicted by three-body models.<sup>17</sup> As a first step away from "effective" two-body models of the  $A=6$  system, it should lead to an assessment of the importance of three-body dynamics. Do three-body models differ significantly from typically used shell models? If so, how? In this work we concentrate on orbital probabilities and wave function shapes, but in the future comparisons with shell-model diagonal and off-diagonal one-body density matrices can be made. Since three-body models are almost always solved in the center-of-mass system with Jacobi coordinates, the shell structure is hidden. Thus, a part of the present paper is our description of the transformation from the Jacobi coordinates to the usual shell-model coordinates with a  $j$ - $j$  coupling.

The text is organized as follows. Section II contains the details of the transformation from Jacobi to shell coordinates. The numerical results for the orbital probabilities and wave function shapes are given in Sec. III, followed in Sec. IV by a discussion and a comparison with the shell models of Table I. The main body of the paper closes in Sec. V with a brief summary and listing of conclusions. Two Appendices give relationships between shell components and three-body wave function components, and a comment about nodes in wave functions, respectively.

## II. TRANSFORMATION TO SHELL CONFIGURATION

We begin with the three-body model bound-state wave functions for  ${}^6\text{Li}$  derived<sup>3,4</sup> from the Schrödinger equation in momentum space and expressed in the Jacobi momenta of the three particles in their center-of-mass system. The Jacobi coordinates for the two nucleons (labeled 1 and 2) and the alpha particle (labeled 3) are shown in Fig. 1. The

symbol  $\vec{k}_{ij}$  will be used for the relative momentum of the  $i$ th and  $j$ th particle, while  $\vec{p}_k$  will represent the relative momentum of the  $k$ th particle with respect to the center of mass of the other two. Any

of the pairs  $(\vec{k}_{12}, \vec{p}_3)$ ,  $(\vec{k}_{23}, \vec{p}_1)$ , or  $(\vec{k}_{31}, \vec{p}_2)$  serve as independent momentum coordinates in the center of mass of the system. The  ${}^6\text{He}(0^+)$  and  ${}^6\text{Li}(1^+)$  ground-state wave functions then take the form<sup>17,18</sup>

$$\begin{aligned} \Psi^{[0]}(\vec{k}_{12}, \vec{p}_3) &= \frac{1}{K_{\text{He}}^2 + k_{12}^2 + \frac{3}{8}p_3^2} (\lambda_0 g_0^0(k_{12}) G^0(p_3) \chi^{[0]}(12)) \\ &\quad + \frac{5}{8} 4\pi \sum_{J=1/2}^{3/2} \sum_{l=J-(1/2)}^{J+1/2} \Lambda_l^J \{ h_l^J(k_{23}) [\mathcal{Y}_{l(1/2)}^{[J]}(\hat{k}_{23}, 2) \times \mathcal{Y}_{l(1/2)}^{[J]}(\hat{p}_1, 1)]^{[0]} F_l^J(p_1) \\ &\quad - (-1)^l h_l^J(k_{31}) [\mathcal{Y}_{l(1/2)}^{[J]}(\hat{k}_{31}, 1) \mathcal{Y}_{l(1/2)}^{[J]}(\hat{p}_2, 2)]^{[0]} F_l^J(p_2) \}, \end{aligned} \quad (3)$$

and

$$\begin{aligned} \Psi_M^{[1]}(\vec{k}_{12}, \vec{p}_3) &= \frac{4\pi}{K_{\text{Li}}^2 + k_{12}^2 + \frac{3}{8}p_3^2} \\ &\quad \times \left[ \lambda_1 \sum_{l, l'=0,2} g_l^1(k_{12}) [[Y^{[l]}(\hat{k}_{12}) \times \chi^{[1]}(12)]^{[1]} \times Y^{[l']}(\hat{p}_3)]_M^{[1]} G^{l'}(p_3) \right. \\ &\quad + \frac{5}{8} \sum_{J=1/2}^{3/2} \sum_{J'=|1-J|}^{1+J} \sum_{l=J-1/2}^{J+1/2} \sum_{l'=J-1/2}^{J+1/2} \frac{1}{2} [1 + (-1)^{l+l'}] \\ &\quad \times \Lambda_l^J \{ h_l^J(k_{23}) [\mathcal{Y}_{l(1/2)}^{[J]}(\hat{k}_{23}, 2) \times \mathcal{Y}_{l'(1/2)}^{[J']}(\hat{p}_1, 1)]_M^{[1]} F_{l'(J')}^{J'}(p_1) \\ &\quad \left. + (-1)^l h_l^J(k_{31}) [\mathcal{Y}_{l(1/2)}^{[J]}(\hat{k}_{31}, 1) \times \mathcal{Y}_{l'(1/2)}^{[J']}(\hat{p}_2, 2)]_M^{[1]} F_{l'(J')}^{J'}(p_2) \right\}, \end{aligned} \quad (4)$$

where

$$\mathcal{Y}_{l(1/2)}^{[J]}(\hat{k}, 2) = \sum_{\mu\eta} \langle l\mu \frac{1}{2}\eta | JM \rangle Y_\mu^{[1]}(\hat{k}) \chi_\eta^{[1/2]}(2).$$

The spectator function  $G^l(p)$  gives the  $l$ -wave momentum distribution of the  $\alpha$  particle relative to the two-nucleon center of mass, while  $F_{l'(J')}^{J'}(p)$  gives the total-angular-momentum ( $J'$ ) and orbital-angular-momentum ( $l'$ ) distributions of a nucleon relative to the center-of-mass of an  $\alpha$ - $N$  pair interacting in a  $l_j$  state. (For the  $0^+$  state, the second pair of indices ( $Jl$ ) on  $F$  are suppressed, since  $J'=J$  and  $l'=l$ .) Note that these angular expansions, convenient for solving the resultant set of coupled integral equations for the spectator functions, are not the shell-model angular expansions in either  $j$ - $j$  or  $\vec{L} \cdot \vec{S}$  formations.

The two-body interactions used in the three-body Schrödinger equation are taken to be separable potentials which best fit the two-body data for binding energy, effective range, scattering length, and phase shifts.<sup>3,4</sup> In momentum space, the  $\alpha N$  interaction is written as

$$\langle \vec{k} | V_{\alpha N} | \vec{k}' \rangle = -\frac{4\pi}{2\mu} \sum_{J=1/2}^{3/2} \sum_{l=J-1/2}^{J+1/2} \Lambda_l^J \hat{J} (-1)^{2J} h_l^J(k) h_l^J(k') [\mathcal{Y}_{l(1/2)}^{[J]}(\hat{k}) \times \mathcal{Y}_{l(1/2)}^{[J]}(\hat{k}')]^{[0]}, \quad (5)$$

with  $\mu = 4M/5$  where  $M$  is the nucleon mass;  $\Lambda_l^J$  is the interaction strength for partial wave  $l$  and total angular momentum  $J$ ;  $\hat{J} \equiv (2J+1)^{1/2}$ ,  $h_l^J(k)$  are form factors analytically represented by  $k^l/[k^2 + (\beta_l^J)^2]^{l+1}$ . For the  $s$ -wave  $NN$  interaction in  ${}^6\text{He}(0^+)$ , only the singlet-spin enters:

$$\langle \vec{k} | V_{nn} | \vec{k}' \rangle = -\frac{\lambda_0}{M} g_0^0(k) g_0^0(k') [\chi^{[0]}(12) \times \tilde{\chi}^{[0]}(12)]^{[0]}, \quad (6)$$

while for  ${}^6\text{Li}(1^+)$ , only the triplet-spin part enters for  $s$  and  $d$  waves:

$$\langle \vec{k} | V_{np} | \vec{k}' \rangle = -\frac{4\pi\lambda_1}{M} \hat{1} \sum_{l,l'=0,2} g_l^1(k) g_{l'}^1(k') [[Y^{[l]}(\hat{k}) \times \chi^{[1]}(12)]^{[1]} \times [Y^{[l']}(\hat{k}') \times \tilde{\chi}^{[1]}(12)]^{[1]}]^{[0]}, \quad (7)$$

with the form factors

$$g_0^S(k) = \frac{1}{k^2 + (\beta_0^S)^2}, \quad g_2^1(k) = \frac{tk^2}{[k^2 + (\beta_1^1)^2]^2}. \quad (8)$$

The parameter  $t$  is used to control the relative strength of the  $d$  wave in the  $np$   $S=1$  interaction, while  $\lambda_0$  and  $\lambda_1$  are the singlet and triplet interaction strengths.

After the spectator functions were found by numerically solving the appropriate integral equations, they were fit to analytic expressions having appropriate threshold and asymptotic behavior.<sup>3,4</sup>

The shell-model wave functions which we generated have as their origin the momentum-space (Jacobi-variable) forms given by Eqs. (3) and (4). Once the basic two-body interactions are set, there are no "free parameters" in the problem. The wave functions in Eqs. (3) and (4) are obtained by solving the three-body Schrödinger equation. To transform Eqs. (3) and (4) into shell-model form, we conform as closely as possible to the spirit of the shell model by taking the alpha particle as the "center-of-force" and "core" of the  ${}^6\text{He}$  and  ${}^6\text{Li}$  nuclei. The four nucleons in the alpha particle fill the  $1s$  shell and, with high probability, remain there as long as available excitation energies are below the alpha-particle disassociation energy ( $\sim 20$  MeV).

In shell-model calculations, it is expedient to assume that the center of force is close to the center of

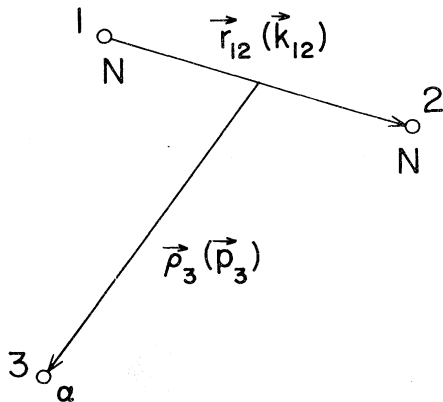


FIG. 1. Jacobi three-body spatial (momentum) coordinates.

mass of the system. This is a questionable assumption for the  ${}^6\text{He}$  and  ${}^6\text{Li}$  nuclei with an alpha-particle core. Our wave functions do not require such an assumption; the wave functions in Eqs. (3) and (4) are the proper three-body ( $\alpha NN$ ) center-of-mass wave functions, so no center-of-mass corrections are required.

In Fig. 2, we show the spatial coordinate vectors  $\vec{r}_1$  and  $\vec{r}_2$  used to locate the two "valence" nucleons. These coordinates are related to the center-of-mass coordinate vectors  $\vec{r}_1$  and  $\vec{r}_2$  and to the Jacobi coordinates  $\vec{r}_{12}$  and  $\vec{p}_3$  (conjugate to  $\vec{k}_{12}$  and  $\vec{p}_3$ ) by

$$\vec{r}_1 = \frac{5}{4} \vec{r}_1 + \frac{1}{4} \vec{r}_2 = -\frac{1}{2} \vec{r}_{12} - \vec{p}_3, \quad (9)$$

$$\vec{r}_2 = \frac{5}{4} \vec{r}_2 + \frac{1}{4} \vec{r}_1 = \frac{1}{2} \vec{r}_{12} - \vec{p}_3 \quad (10)$$

with the invariant

$$\begin{aligned} \sum_{i=1}^3 \vec{r}_i \cdot \vec{p}_i &= \vec{r}_{12} \cdot \vec{k}_{12} + \vec{p}_3 \cdot \vec{p}_3 \\ &= \vec{r}_1 \cdot \vec{p}_1 + \vec{r}_2 \cdot \vec{p}_2. \end{aligned}$$

The shell waves we have calculated are found by Fourier transforming the momentum-space wave functions and expanding into shell angular states with "j-j" coupling, i.e., into states for which each of the valence nucleons has definite total angular momentum. This expansion can be expressed as

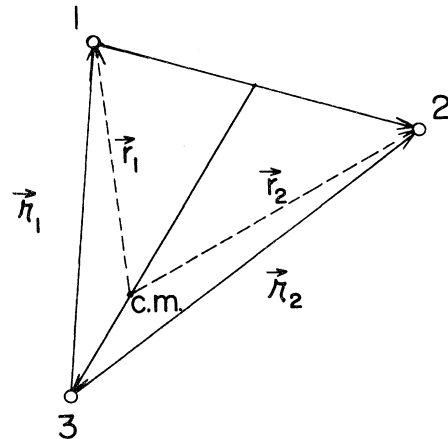


FIG. 2. Shell, Jacobi, and center-of-mass spatial coordinates.

$$\Psi_M^{[J]}(\vec{\mu}_1, \vec{\mu}_2) = \sum_{\substack{J_1 J_2 \\ L_1 L_2}} \mathcal{S}_{L_1 L_2}^{J_1 J_2}(\mu_1, \mu_2) [\mathcal{Y}_{L_1(1/2)}^{[J_1]}(\hat{\mu}_1, 1) \times \mathcal{Y}_{L_2(1/2)}^{[J_2]}(\hat{\mu}_2, 2)]_M^{[J]}. \quad (11)$$

The  $\mathcal{S}_{L_1 L_2}^{J_1 J_2}(\mu_1, \mu_2)$  are the two-body configuration-space amplitudes for finding the valence nucleons in the indicated angular state relative to the  $\alpha$ -particle core.

With the identity

$$e^{i\vec{k}\cdot\vec{r}} = 4\pi \sum_{l=0}^{\infty} i^l j_l(kr) \hat{l} [Y^{[l]}(\hat{k}) \times Y^{[l]}(\hat{r})]^{[0]}, \quad (12)$$

where  $j_l(kr)$  is a spherical Bessel function, we can solve for the  $\mathcal{S}$ 's in terms of  $\Psi_M^{[J]}(\vec{k}, \vec{p})$ :

$$\begin{aligned} \mathcal{S}_{L_1 L_2}^{J_1 J_2}(\mu_1, \mu_2) = & (-1)^{(L_1+L_2)/2} \frac{(4\pi)^2}{\hat{J}} \int \int \frac{d^3 p_1 d^3 p_2}{(2\pi)^3} j_{L_1}(p_1 \mu_1) j_{L_2}(p_2 \mu_2) \\ & \times [[\tilde{\mathcal{Y}}_{L_1(1/2)}^{[J_1]}(\hat{p}_1, 1) \times \tilde{\mathcal{Y}}_{L_2(1/2)}^{[J_2]}(\hat{p}_2, 2)]^{[J]} \times \Psi^{[J]}(\vec{k}, \vec{p})]^{[0]}. \end{aligned} \quad (13)$$

There are two technical difficulties with the numerical implementation of the above expression. First, there are literally hundreds of angular recoupling terms that must be included. Second, the integrals over  $p_1$  and  $p_2$  involve strongly oscillatory integrands for  $pr \gg 1$ . In the normalization integral used to check the numerics,

$$\sum_{\substack{J_1 J_2 \\ L_1 L_2}} \int_0^{\infty} \int_0^{\infty} |\mathcal{S}_{L_1 L_2}^{J_1 J_2}(\mu_1, \mu_2)|^2 \mu_1^2 d\mu_1 \mu_2^2 d\mu_2 = 1, \quad (14)$$

there will be an implicit fivefold integration required. Thus an efficient and accurate numerical scheme is needed for handling the integrals over spherical Bessel functions.

The first difficulty is made manageable by the graphical recoupling method of Danos.<sup>19,3</sup> The second motivated our work with Maximon,<sup>20</sup> where we developed a powerful method of integrating numerically an integrand containing a spherical Bessel function by use of product integration.

In Appendix A, we give the results of the angular reduction of the integrand of Eq. (13) for both  ${}^6\text{He}(0^+)$  and  ${}^6\text{Li}(1^+)$ . In this work, we include all shell waves up to  $L=2$  (higher  $L$  waves have negligible contribution to the normalization integral) by evaluating the expressions in Appendix A.

After numerical evaluation of Eq. (13), besides  $\mathcal{S}_{L_1 L_2}^{J_1 J_2}(\mu_1, \mu_2)$ , we have calculated the two-particle probability densities  $|\mathcal{S}_{L_1 L_2}^{J_1 J_2}(\mu_1, \mu_2)|^2$ , the single-particle radial densities

$$P_{L_1 L_2}^{J_1 J_2}(\mu_1) = \mu_1^2 \int_0^{\infty} \mu_2^2 d\mu_2 |\mathcal{S}_{L_1 L_2}^{J_1 J_2}(\mu_1, \mu_2)|^2, \quad (15)$$

and the probabilities of the shell orbitals,

$$P_{L_1 L_2}^{J_1 J_2} = \int_0^{\infty} P_{L_1 L_2}^{J_1 J_2}(\mu_1) d\mu_1. \quad (16)$$

Of course,

$$\sum_{\substack{J_1 J_2 \\ L_1 L_2}} P_{L_1 L_2}^{J_1 J_2} = 1 \quad (17)$$

from Eq. (14). Note that, as we do not assume any particular shell-core potential, we have no "principal" or "radial" quantum number. However, since our expansion is dominated by the  $s$ ,  $p$ , and  $d$  angular shell states just outside the alpha-particle core, we expect these states to correspond to the  $2s$ ,  $1p$ , and  $1d$  states in any shell model, with little or no admixture from higher radial shells. This expectation is fulfilled by the observation of the correct number of radial nodes in the calculated waves, i.e., one node for the  $s$  wave and none for the  $p$  or  $d$  waves.

### III. NUMERICAL RESULTS

Several different  ${}^6\text{He}$  and  ${}^6\text{Li}$  three-body wave functions are used in our examination of the  $A=6$  shell structure as predicted by three-body models. They differ through the  $NN$  and  $\alpha N$  interactions used to derive them. In Table II, where certain properties are listed for the wave functions considered, the main division of models is "simple" and "full." This distinction pertains to the  $\alpha N$  interaction, wherein the full models are derived by inclusion of *all* the dominant low energy partial waves of the  $\alpha N$  interaction, i.e.,  $S_{1/2}$ ,  $P_{1/2}$ , and  $P_{3/2}$ , while the simple model includes only the resonant  $P_{3/2}$  interaction. For  ${}^6\text{He}$ , the parenthetical  $nn$  or  $np$  indicates which set of  $NN$  low-energy parameters

TABLE II. Wave function models.

Model	Wave function	Binding energy (MeV)	${}^6\text{He}$ $\beta$ -decay $ft$ value(s) (Ref. 7)	Ref.
Simple	${}^6\text{He}$	1.043		3
	${}^6\text{Li}(0\%)$	4.660	$834 \pm 13$	6
Full	${}^6\text{He}(nn)$	0.359		3
	${}^6\text{He}(np)$	0.542		3
	${}^6\text{Li}(0\%)$	4.446	$790 \pm 12^a$	4
	${}^6\text{Li}(4\%)$	4.062	$807 \pm 12^a$	4
	${}^6\text{Li}(4\%; t=0)$	4.062	$779 \pm 12^a$	4
Experiment	${}^6\text{He}$	0.969		
	${}^6\text{Li}$	4.531	$807 \pm 2$	

<sup>a</sup>Calculated with the  ${}^6\text{He}(np)$  wave function.

were used to derive the  ${}^1S_0$  interaction. The parenthetical percentage attached to the models is the percentage  $d$ -state component in the deuteron wave function derived from the  ${}^3S_1$ - ${}^3D_1$  interaction used. Finally, the  ${}^6\text{Li}$  model labeled (4%;  $t=0$ ) is the same three-body wave function as (4%), but the terms that contain explicitly the two-nucleon tensor form factors,  $g_1^2(k)$ , have been dropped and the wave function renormalized. Thus, the effect of the explicit tensor-force terms can be examined. Details for all of these models, e.g., interaction parameters, spectator-function tabulations, etc., can be found in Refs. 3, 4, and 7.

The calculated orbital probabilities [Eqs. (16) and (17)] for  ${}^6\text{He}$  and  ${}^6\text{Li}$  are given in Tables III and IV, respectively. They are labeled and ordered according to standard shell-model  $j$ - $j$  coupling, i.e.,  $p$  shell, ( $s$ - $d$ ) shell, etc. By a number of sensitivity tests on our numerical integrations, we have concluded that the orbital probability values are stable to within 3 parts in 1000. It is clear from the tables that simple and full models differ markedly from each other, and that the bulk of the wave function probability resides in the  $p$  shell with essentially all of the remainder coming from the ( $s$ - $d$ ) shell. Clearly, the sum of the orbital probabilities through the ( $s$ - $d$ )

shell is well converged ( $\geq 95\%$ ). The orbital probabilities are obtained by integrating over the single-particle radial (orbital) densities [Eq. (15)]. Simple and full model graphs of these densities are given for  ${}^6\text{He}$  and  ${}^6\text{Li}$  in Figs. 3 and 4, respectively. At this level, one can clearly distinguish between the simple and full model orbital probabilities. Numerically, the single-particle orbital densities are stable to within 1 part in 100 between 1 and 8 fm, although there is more variance in the  $d$ -wave results for small and large  $\kappa$  due to the small relative size of these densities in those regions.

Effects in the models for the single-particle radial densities due to the different  $NN$  interactions are brought out in Figs. 5–13. Figures 5–7 show the differences between the three  ${}^6\text{He}$  models for the  $p_{3/2}$ ,  $d_{5/2}$ , and  $s_{1/2}$  orbitals, respectively. Representative graphs contrasting simple  ${}^6\text{Li}$  (4%) and  ${}^6\text{Li}$  (4%,  $t=0$ ) models are given in Figs. 8–11. Specifically chosen are the  $p_{3/2}(p_{3/2})$ ,  $s_{1/2}(d_{3/2})$ ,  $d_{3/2}(s_{1/2})$ , and  $d_{5/2}(d_{5/2})$  orbital densities. Differences between  ${}^6\text{Li}$  (0%) and  ${}^6\text{Li}$  (4%) are shown for the  $p_{3/2}(p_{3/2})$  and  $p_{1/2}(p_{3/2})$  orbitals in Figs. 12 and 13.

With the above results, we are now ready to discuss the physics of the models.

#### IV. DISCUSSION

To understand differences between the simple and full models, a few comments about the  $\alpha N$  interactions are useful. The  $P_{3/2}$  and  $P_{1/2}$  interactions are both attractive, but unlike the strongly resonant  $P_{3/2}$  wave, the  $P_{1/2}$  is nonresonant and less important in binding together the  $A=6$  bound states.<sup>3,4</sup> On the other hand, the  $S_{1/2}$  wave must contain the physics of the Pauli principle, i.e., the  $S_{1/2}$  interaction must repel the nucleon from the alpha particle when they begin to approach each other too closely. In the

TABLE III. Orbital probabilities ( ${}^6\text{He}$ )  $\times 100\%$ .

Orbital	Simple model	Full ( $nn$ )	Full ( $np$ )
$(p_{3/2})^2$	79.1	86.1	85.6
$(p_{1/2})^2$	1.95	3.55	3.83
$(d_{5/2})^2$	4.58	4.15	4.34
$(s_{1/2})^2$	10.95	3.19	3.18
$(d_{3/2})^2$	1.14	1.12	1.21
Sum	97.7	98.1	98.2

TABLE IV. Orbital probabilities ( ${}^6\text{Li}$ ) $\times 100\%$ .

Orbital	Simple model	Full (0%)	Full (4%)	Full (4%; $t=0$ )
$(p_{3/2})^2$	49.2	51.1	44.7	48.1
$(p_{1/2}p_{3/2})$	14.8	30.2	33.8	32.6
$(p_{1/2})^2$	0.7	1.5	0.5	1.2
$(d_{5/2})^2$	3.9	4.3	3.3	4.1
$(s_{1/2})^2$	20.1	5.4	5.5	5.8
$(s_{1/2}d_{3/2})$	0.1	0.0	0.2	0.2
$(d_{5/2}d_{3/2})$	4.8	6.6	7.8	6.8
$(d_{3/2})^2$	0.5	0.8	0.3	0.7
Sum	94.1	99.9	96.1	99.5

models under consideration, the  $S_{1/2}$  interaction is purely repulsive and gives an excellent representation of the  $S_{1/2}$  phase shift.<sup>3,4</sup> Therefore, the dominant pieces in the  $\alpha N$  interaction are the  $P_{3/2}$  wave,

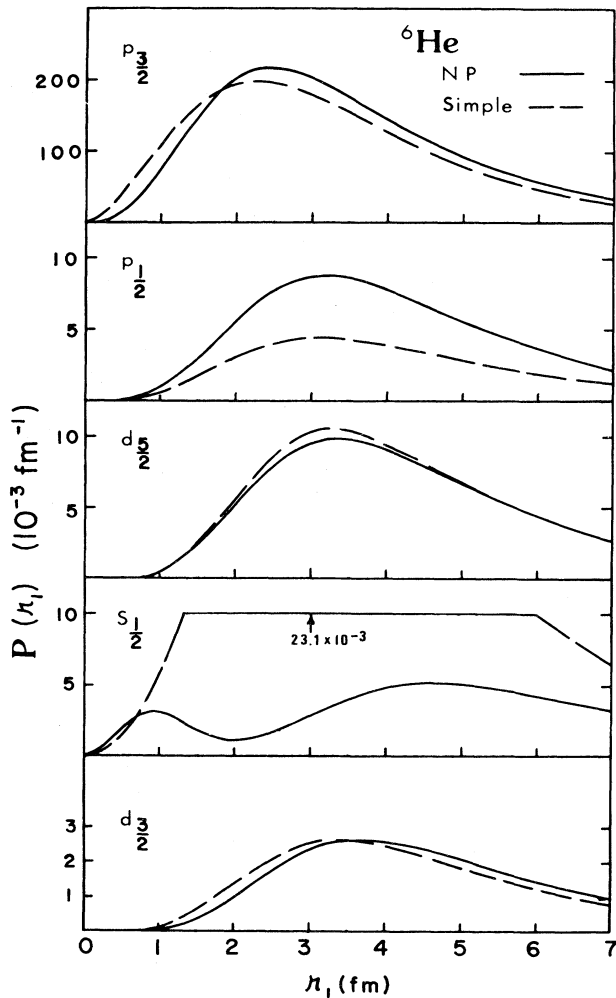


FIG. 3.  ${}^6\text{He}$  single-particle radial densities  $[P_{L_1 L_2}^{J_1 J_2}(\mu)]$ . Simple model ( $S$ ) and full ( $np$ ) model ( $NP$ ).

which provides the bulk of the attraction, and the  $S_{1/2}$  wave, which counters the  $P$ -wave attraction with repulsion whose origin is the Pauli principle. So the essence of the difference between the simple and full models is that the simple model does not contain the required physics of the Pauli exclusion principle through the  $\alpha N$  interaction. As we shall see, this is a serious shortcoming of the simple model.

When we consider the orbital probabilities for  ${}^6\text{He}$  and  ${}^6\text{Li}$  in Tables III and IV, respectively, we see that the absence of the  $S_{1/2}$   $\alpha N$  repulsion in the simple model leads to a  $(s_{1/2})^2$  orbital probability almost four times that predicted by the full models. The large  $(s_{1/2})^2$  probability is obtained at the expense of the  $p$ -shell probability, particularly the  $(p_{3/2})^2$  for  ${}^6\text{He}$  and  $(p_{1/2}p_{3/2})$  for  ${}^6\text{Li}$ . Moreover, as we shall see below when we consider the single-particle radial densities, this large  $(s_{1/2})^2$  probability originates from an  $s$ -wave orbital density that has a  $1s$  rather than  $2s$  [for the  $(s-d)$  shell] form, in violation of the filling of shells according to the Pauli principle. Beyond this striking difference between the simple- and full-model orbital probabilities, the remaining differences between the simple and full models are insignificant.

Besides the simple and full models, there are different  $NN$  interactions used within the full models. At least for the orbital probabilities, whether we use the  $nn$  or  $np$   ${}^1S_0$  interaction for  ${}^6\text{He}$  is of no significance. The tensor force does have an effect in  ${}^6\text{Li}$ . It redistributes some of the  $(p_{3/2})^2$  probability into other orbits. This redistribution of probability is most likely a consequence of the  $\sim 0.4$  MeV reduction in binding energy from full (0%) to full (4%). Its source is the explicit tensor force terms in the wave function as can be seen from the full (4%;  $t=0$ ) column, whereby dropping these terms we move back towards full (0%).

Globally, the  $A=6$  orbital probabilities reflect the underlying  $\alpha N$  interactions. The dominance of the

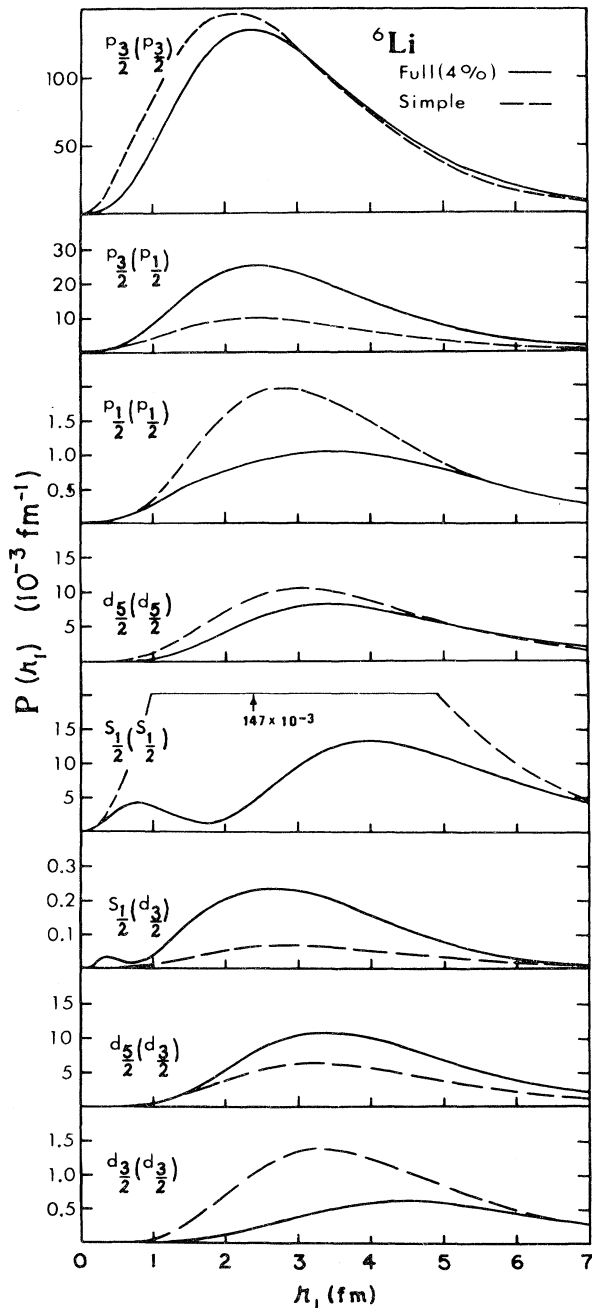


FIG. 4.  ${}^6\text{Li}$  single-particle radial densities  $[P_{L_1 L_2}^{J_1 J_2}(\rho)]$ . Simple model (S) and full (4%) model (F).

$(p_{3/2})^2$  in  ${}^6\text{He}$  and the  $(p_{3/2})^2$  plus  $(p_{1/2}p_{3/2})$  in  ${}^6\text{Li}$  has its source in the resonant  $P_{3/2} \alpha N$  interaction. The  $(p_{1/2})^2$  component is small, compatible with the much lesser role played by the  $P_{1/2} \alpha N$  interaction. Additionally, as we learned above, the  $(s_{1/2})^2$  component is suppressed due to the repulsive  $S_{1/2} \alpha N$  interaction. Nuances to these gross features must

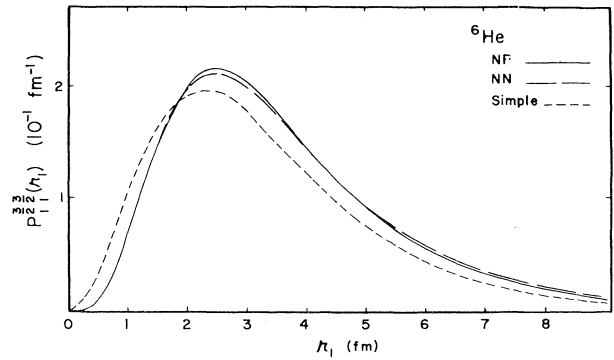


FIG. 5.  ${}^6\text{He}$  single-particle  $p_{3/2}(p_{3/2})$  radial density for the three models discussed in the text.

have their origin in the  $NN$  interaction—the interaction that makes the physics a three-body bound-state problem.

Comparison of the three-body-model orbital probabilities with those from the phenomenological and realistic-interaction shell models discussed in the Introduction is striking (see Table V). First, for  ${}^6\text{He}$  (Table III) the distribution of probability across the orbitals of the  $p$  shell for the two full three-body models only comes close to the realistic-interaction shell model results III of Vergados. These shell models include core excitation ( $2p + 3p - 1h + 4p - 2h$ ). Thus, core excitation tends to produce a distribution of orbital probabilities in an “effective” two-body model that resembles that from a three-body model where the alpha-particle core is inert. This implies that *three-body dynamical effects could be misinterpreted as requiring core excitations in “effective” two-body theories*. Although this similarity does exist, the three-body models do not assign as much probability to the  $(p_{1/2})^2$  orbital as the shell models III(a) and III(b). Second, *none* of the shell models for  ${}^6\text{Li}$  in Table V have a distribution

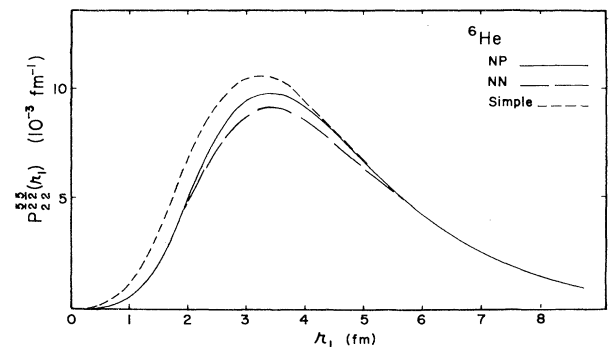


FIG. 6.  ${}^6\text{He}$  single-particle  $d_{5/2}(d_{5/2})$  radial density for the three models discussed in the text.

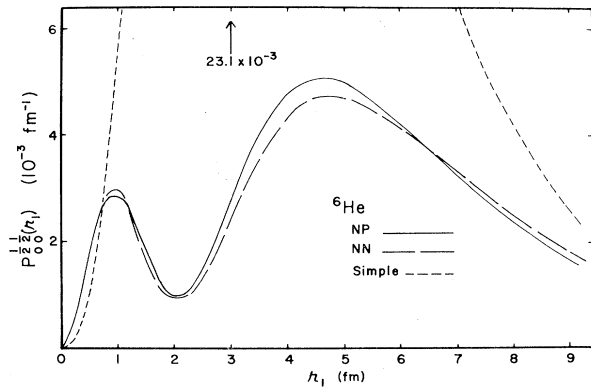


FIG. 7.  ${}^6\text{He}$  single-particle  $s_{1/2}(s_{1/2})$  radial density for the three models discussed in the text.

of orbital probabilities in the  $p$  shell that resemble the full three-body results (Table IV). The critical aspect seems to be that when the shell models reduce the  $(p_{3/2})^2$  probability to values comparable to three-body models, the  $(p_{1/2}p_{3/2})$  probability becomes  $\sim 30$  to  $50\%$  greater than in the full three-body models. Said differently, the  $(s-d)$  shell plays a larger role in  ${}^6\text{Li}$  for three-body models than it does in these shell models.<sup>21</sup> So, even at this fully integrated level—orbital probabilities—distinctive differences between shell models and three-body models of the  $A = 6$  system stand out.

One step down from the orbital probabilities is the single-particle orbital densities, Eq. (15). In Figs. 3 and 4, the simple- and full- ( $np$  for  ${}^6\text{He}$  and  $4\%$  for  ${}^6\text{Li}$ ) model single-particle densities for  ${}^6\text{He}$  and  ${}^6\text{Li}$ , respectively, are compared for all orbitals through the  $(s-d)$  shell. The differences are vivid. The relative sizes of the two models for each orbital is reflected in the orbital probabilities (Tables III and IV), while the trend of the full models to peak at a

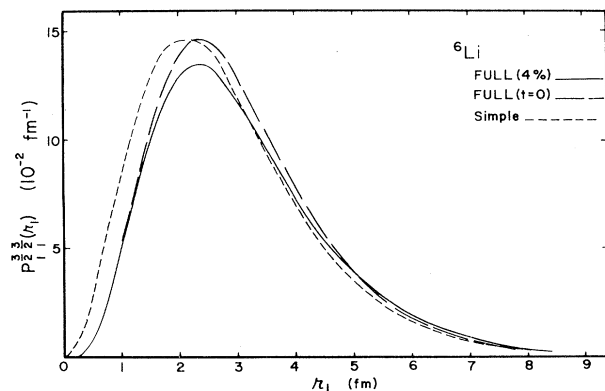


FIG. 8.  ${}^6\text{Li}$  single-particle  $p_{3/2}(p_{3/2})$  radial density for the simple, full (4%), and full (4%,  $t = 0$ ) models.

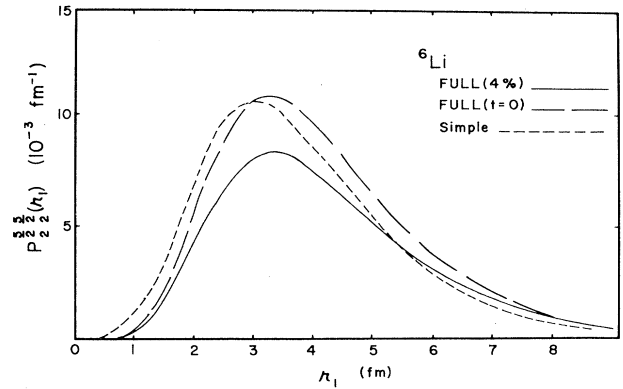


FIG. 9.  ${}^6\text{Li}$  single-particle  $d_{5/2}(d_{5/2})$  radial density for the simple, full (4%), and full (4%,  $t = 0$ ) models.

greater radial distance occurs because their three-body binding energies are less than for the simple models (See Table II). One particular feature of note is the structure of the  $s_{1/2}(s_{1/2})$  [also the  $s_{1/2}(d_{3/2})$  for  ${}^6\text{Li}$ ] orbitals for the two models. The full-model  $s_{1/2}(s_{1/2})$  densities approach a zero at  $\sim 2$  fm, whereas the simple-model results are near a maximum at this point. The tendency towards a zero (node) in the single-particle orbital density can be traced to the fact that the  $s_{1/2}(s_{1/2})$  two-body configuration-space amplitude has a node (See Appendix B). The absence of this minimum for the simple model is evidence that the  $s_{1/2}(s_{1/2})$  wave function has  $1s$  behavior rather than the expected  $2s$  behavior required by the Pauli principle. On these grounds, it is clear that the neglect of the  $S_{1/2} \alpha N$  interaction in the simple model is unjustified. Finally, we note that the maxima of the single-particle orbital densities order the orbits within shells, i.e., for  ${}^6\text{He}$  (full model), the maxima occur at  $\sim 2.4$  fm for

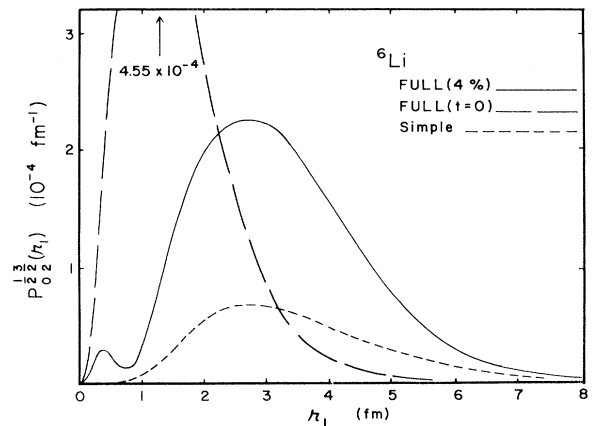


FIG. 10.  ${}^6\text{Li}$  single-particle  $s_{1/2}(d_{3/2})$  radial density for the simple, full (4%), and full (4%,  $t = 0$ ) models.

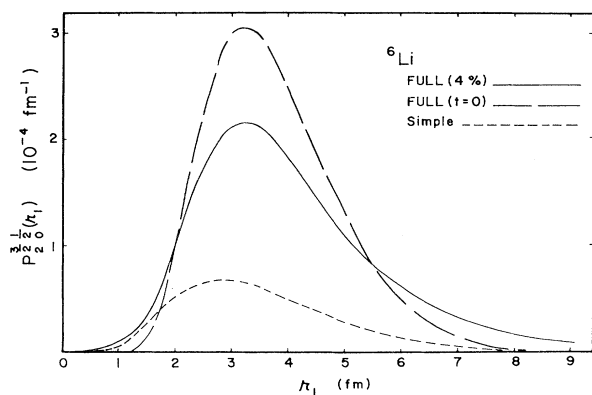


FIG. 11.  ${}^6\text{Li}$  single-particle  $d_{3/2}(s_{1/2})$  radial density for the simple, full (4%), and full (4%,  $t=0$ ) models.

$p_{3/2}(p_{3/2})$ ,  $\sim 3.2$  fm for  $p_{1/2}(p_{1/2})$ ,  $\sim 3.4$  fm for  $d_{5/2}(d_{5/2})$ , and  $\sim 3.7$  fm for  $d_{3/2}(d_{3/2})$ ; the situation is similar for  ${}^6\text{Li}$ . Ordering of the  $s_{1/2}(s_{1/2})$  orbital relative to other orbitals requires knowledge of the rms orbital radii:

$$\langle r^2 \rangle_{L_1 L_2}^{J_1 J_2} = \int_0^\infty r_1^2 P_{L_1 L_2}^{J_1 J_2}(r_1) dr_1. \quad (18)$$

The results are given in Table VI. This ordering of orbitals, or equivalently the different shape of each single-particle orbital density within a shell, is a distinctive feature of three-body models and it emphasizes the role of the three-body dynamics as generated by the underlying two-body  $\alpha N$  and  $NN$  interactions.<sup>22</sup>

Do the single-particle orbital densities display large differences owing to the different  $NN$  interactions? Figures 5–7 show the single-particle densities

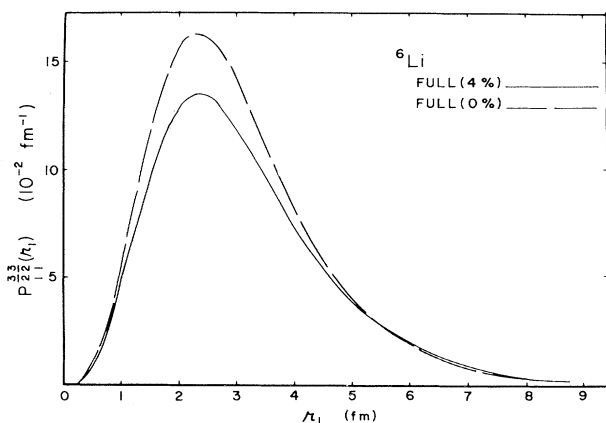


FIG. 12.  ${}^6\text{Li}$  single-particle  $p_{3/2}(p_{3/2})$  radial density for the full (4%) and full (0%) models.

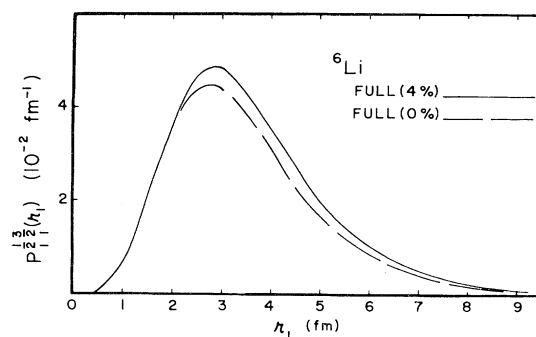


FIG. 13.  ${}^6\text{Li}$  single-particle  $p_{1/2}(p_{3/2})$  radial density for the full (4%) and full (0%) models.

ties for the  ${}^6\text{He}$   $p_{3/2}(p_{3/2})$ ,  $d_{5/2}(d_{5/2})$ , and  $s_{1/2}(s_{1/2})$  orbitals. Little difference appears between the full ( $nn$ ) and full ( $np$ ) models. What difference there is can be attributed to the smaller three-body binding energy in the full ( $nn$ ) case (Table II). On the other hand, the presence of the tensor force in the  $NN$  interaction has a significant effect on the single-particle densities for  ${}^6\text{Li}$  as can be seen in Figs. 8–13, especially for the ( $s$ - $d$ ) shell. In Figs. 8–11, the simple, full (4%), and full (4%,  $t=0$ ) models are compared for the  $p_{3/2}(p_{3/2})$ ,  $d_{5/2}(d_{5/2})$ ,  $d_{3/2}(s_{1/2})$ , and  $s_{1/2}(d_{3/2})$  orbitals. In all cases, the effect of the explicit tensor-force terms is to reduce the densities and change their shape. Such aspects can be expected to be important in computing the  ${}^6\text{Li}$  quadrupole moment where the smaller components of the wave function play an important role.<sup>6</sup> This effect of the tensor force is again seen in Figs. 12 and 13 where the full (0%) and full (4%)  $p_{3/2}(p_{3/2})$  and  $p_{1/2}(p_{3/2})$  orbitals are given, respectively.

Again, let us return to comparing the shell model and three-body models, but now for the single-particle densities. As representative examples, we compare the  $p_{3/2}(p_{3/2})$  and  $p_{1/2}(p_{1/2})$  orbitals of  ${}^6\text{He}$  in Figs. 14 and 15, respectively. The shell model is that of Donnelly and Walecka (DW). Two main aspects should be noted.

(1) The three-body model predicts an exponentially decaying density at large radial distances. Thus, rather than the compact Gaussian shape of the oscillator shell model, the density has an exponential tail.

(2) The oscillator shell model indicates the same location for the maxima of the  $p_{3/2}(p_{3/2})$  and  $p_{1/2}(p_{1/2})$  orbitals, whereas the three-body model predicts that they are ordered. Both of these aspects can have significant bearing on the calculations of observable quantities. On the other hand, it can be argued that these shortcomings of the oscillator wave functions are overcome by generating single-

TABLE V. Orbital probabilities ( $\times 100\%$ ) from phenomenological and realistic-interaction shell models of Table I.

Source	${}^6\text{Li}$				Sum	${}^6\text{He}$		Sum
	$A^2$	$B^2$	$C^2$	$E^2$				
DW	65.6	33.7	0.7		100	64.0	36.0	100
BAH								
Saskatoon <i>A</i>	65.6	33.7	0.7		100	99.6	0.2	99.8
Saskatoon <i>B</i>	65.6	33.7	0.7		100	66.6	33.3	99.9
Vergados								
I(a)	63.8	36.0	0.06		99.9	95.6	4.2	99.8
(b)	54.3	45.6	0.02		99.9	91.8	8.0	99.8
II(a)	55.2	39.6	0.07		94.9	93.9	4.2	98.1
(b)	46.6	47.7	0.03		94.3	91.6	6.0	97.6
III(a)	53.1	38.3	0.07		91.5	88.5	4.6	93.1
(b)	45.2	45.4	0.04		90.6	86.3	6.4	92.7

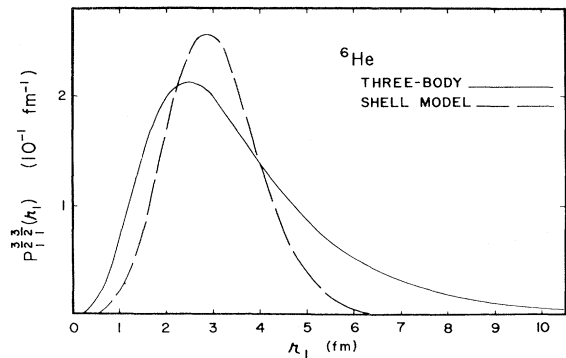
particle orbital densities from Woods-Saxon wave functions. Woods-Saxon wave functions decay exponentially at large distances and order the orbits through the spin-orbit interaction. In fact, the parameters of the Woods-Saxon potential can be chosen to yield a wave function with the same separation energy as that implicit in the three-body single-particle orbital density and the resulting wave function can be normalized to yield the same orbital probability as the three-body prediction. Will the single-particle orbital density then resemble closely that of the three-body prediction? The answer is apparent in Fig. 16, where the  ${}^6\text{He}$  full ( $nn$ ) model and a Woods-Saxon  $1p_{3/2}$  single-particle orbital density are compared. The normalization and separation energy of the Woods-Saxon model are the same as in the three-body model. The Woods-Saxon density is narrower, peaks at a larger radial distance, and in the region from 0 to  $\sim 5$  fm resembles more the oscillator density (See Fig. 14). Clearly, for typical values of the radius and diffuseness in the Woods-Saxon potential, the physics of the three-body

models differs not only from the usual oscillator models, but from the Woods-Saxon effective two-body models as well.<sup>23</sup>

Simple oscillator shell models and all three-body models differ in another way: The two-body configuration-space wave function amplitude  $\mathcal{P}_{L_1 L_2}^{J_1 J_2}(\kappa_1, \kappa_2)$  does not factor in three-body models. This amplitude, of course, underlies everything we discussed above, so it would be most valuable to see it plotted for two representative cases. We have chosen the  ${}^6\text{He}$   $(p_{3/2})^2$  and  $(s_{1/2})^2$  amplitudes. They are displayed in Figs. 17–20 as three-dimensional and contour plots. The  $(p_{3/2})^2$  amplitude shows a strong peak at  $\kappa_1 = \kappa_2 \sim 2$  fm, whose origin, we learned above, is the strongly resonant  $p_{3/2}$   $\alpha N$  interaction. The smoothness of the curves in the contour plots at large radial distances is a measure of the accuracy of our results. Poor numerical accuracy leads to undulating contours at large distances. Most importantly, we note the node in the  $(s_{1/2})^2$

TABLE VI. Root-mean-square orbital radii (fm).

Orbital	${}^6\text{He}(np)$	${}^6\text{Li}$ (4%)
$(p_{3/2})^2$	4.29	3.53
$p_{3/2}(p_{1/2})$		3.62
$p_{1/2}(p_{3/2})$		3.97
$(p_{1/2})^2$	4.98	4.61
$(d_{5/2})^2$	5.20	4.66
$d_{5/2}(d_{3/2})$		4.58
$d_{3/2}(d_{5/2})$		4.66
$(s_{1/2})^2$	6.37	5.04
$s_{1/2}(d_{3/2})$		4.42
$d_{3/2}(s_{1/2})$		3.51
$(d_{3/2})^2$	5.56	5.67

FIG. 14.  ${}^6\text{He}$  single-particle  $p_{3/2}(p_{3/2})$  radial density for the full ( $np$ ) three-body model and the Donnelly-Walecka shell model.

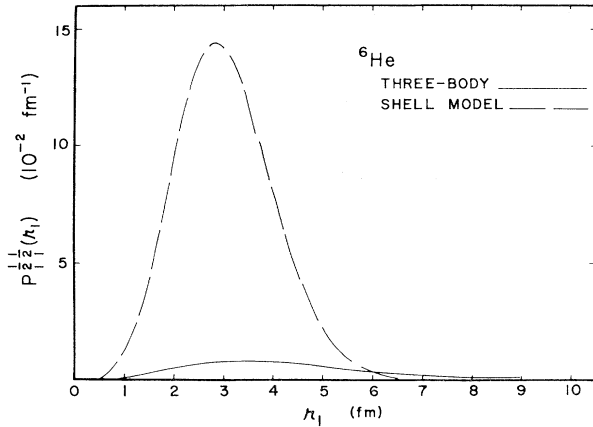


FIG. 15.  ${}^6\text{He}$  single-particle  $p_{1/2}(p_{1/2})$  radial density for the full  $(np)$  three-body model and the Donnelly-Walecka shell model.

amplitude, the origin of which is the repulsive  $S_{1/2}$   $\alpha N$  interaction. This node demonstrates the true  $2s$  character of the  $(s_{1/2})^2$  single-particle densities and amplitudes in the full models. This result complements very nicely the diffraction minimum predicted in the  ${}^6\text{Li} \rightarrow \alpha + d$  momentum distribution by three-body models.<sup>6</sup> The diffraction minimum has

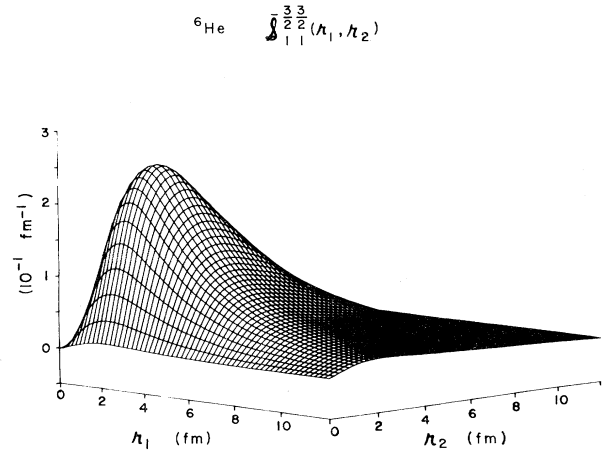


FIG. 17.  ${}^6\text{He}$  full  $(np)$  model  $(p_{3/2})^2$  two-body configuration-space reduced wave-function amplitude,  $\mathcal{F} = \kappa_1 \kappa_2 \mathcal{L}$ .

the same source: the Pauli exclusion principle.

With the three-body model predictions of the shell angular amplitudes in hand, direct comparison can be made with shell model predictions. For example, as Donnelly<sup>24</sup> has pointed out, the one body transition densities

$$\rho_{(s, \mathcal{F}) \mathcal{L} M_{\mathcal{L}}}^{(J' T'; J T)}(\vec{\kappa}'_1, \vec{\kappa}_1) \equiv 6 \sum_{\substack{\text{spin} \\ \text{isospin} \\ m's}} \int \cdots \int_{\vec{r}_2 \text{ to } \vec{r}_6} [X^{[s; \mathcal{F}]}(1) \times [\Psi^{[J', T']}(r'_1 \cdots) \times \tilde{\Psi}^{[J, T]}(r_1 \cdots)]^{[\mathcal{F}; \mathcal{F}]}]_{M_{\mathcal{L}}}^{[\mathcal{L}]}, \quad (19)$$

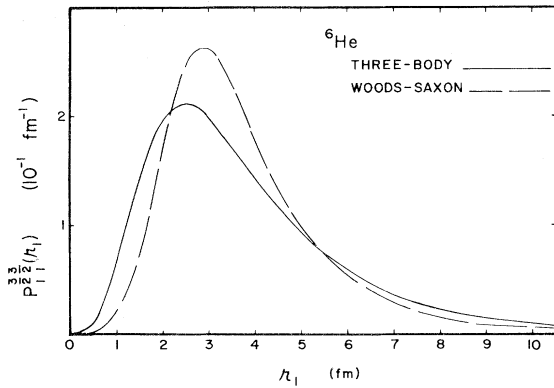


FIG. 16.  ${}^6\text{He}$  single-particle  $p_{3/2}(p_{3/2})$  radial density for the full  $(nn)$  three-body model and a Woods-Saxon wave function. The Woods-Saxon wave function has the same separation energy (0.9465 MeV) and normalization (0.861) as the three-body model. For values of  $r \geq 11$  fm, the ratio of the two densities approaches a constant. The parameters of the Woods-Saxon potential are  $V_c = 27.12$  MeV,  $V_{s0} = 5$  MeV,  $a = 0.5$  fm, and  $R = 3.1$  fm, with a reduced mass of 782.2 MeV.

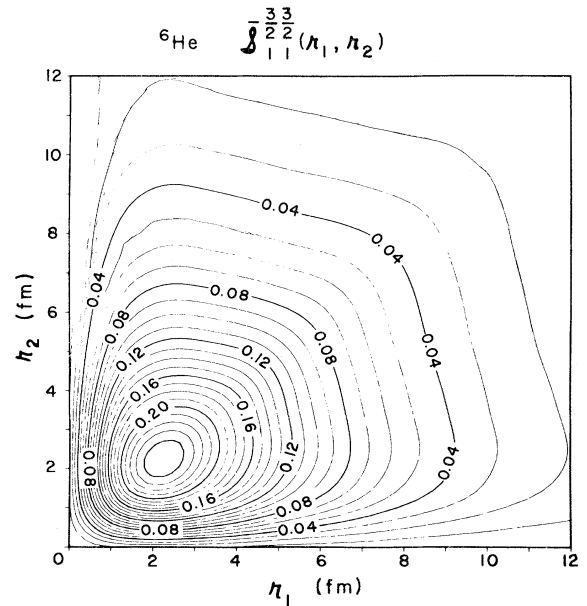


FIG. 18. Contour plot of amplitude given in Fig. 17.

where

$$X_m^{[\mathcal{J}]}(i) = \sigma_{m_s}^{[\mathcal{J}]}(i) \mathcal{S}_{m_s}^{[\mathcal{J}]}(i) \tag{20}$$

and

$$\sigma_{m_s}^{[\mathcal{J}]} = 1 \text{ for } \mathcal{J}=0; \quad -i\sigma_{m_s} \text{ for } \mathcal{J}=1, \tag{21}$$

contain all nuclear structure information which determines single nucleon transitions. These densities can be calculated directly from the shell angular amplitudes  $\mathcal{S}$ :

$$\begin{aligned} \rho_{(\mathcal{J}, \mathcal{S})}^{(J'T'; JT)}(\vec{r}_1, \vec{r}_2) = & 6 \sum_{\substack{j_1' l_1' \\ j_1 l_1 \\ j_2 l_2}} (-1)^{j_1+j_2+J+\mathcal{S}+1+T'+\mathcal{S}} \widehat{\mathcal{S}} \widehat{T} \widehat{T}' \left(\frac{1}{2}\right)^2 \widehat{\mathcal{J}} \widehat{\mathcal{J}}' \widehat{j}_1 \widehat{j}_1' \widehat{\mathcal{J}} \\ & \times \begin{bmatrix} T & T' & \mathcal{S} \\ \frac{1}{2} & \frac{1}{2} & \frac{1}{2} \end{bmatrix} \begin{bmatrix} J' & J & \mathcal{J} \\ j_1 & j_1' & j_2 \end{bmatrix} \begin{bmatrix} l_1' & \frac{1}{2} & j_1' \\ l_1 & \frac{1}{2} & j_1 \\ \mathcal{L} & s & \mathcal{J} \end{bmatrix} [Y^{[l_1']}(r_1') \times Y^{[l_1]}(r_1)]_{m_s}^{[\mathcal{L}]} \\ & \times \int r_2^2 dr_2 \mathcal{S}_{l_1' l_2}^{j_1' j_2(J)}(r_1, r_2) \mathcal{S}_{l_1 l_2}^{j_1 j_2(J)}(r_1, r_2). \end{aligned} \tag{22}$$

We leave such comparisons for the future.

V. SUMMARY AND CONCLUSIONS

In this paper, we have investigated the shell structure of the  $A=6$  bound states,  ${}^6\text{He}$  and  ${}^6\text{Li}$ , as it is predicted by three-body models. Our main objective was to assess the importance of three-body dynamics as compared to “effective” two-body models such as the phenomenological and the realistic-interaction shell models. Comparisons were made between three-body-model and shell-model predictions for orbital probabilities, single-particle orbital densities, and two-body wave function amplitudes in  $j$ - $j$  cou-

pling. Within the context of the three-body models alone, the role of the basic interactions, i.e.,  $\alpha N$  and  $NN$ , in determining the predicted shell structure was thoroughly examined. Overall, at this level, it is clear that shell structure predicted by three-body models of the  $A=6$  bound states differs, and in some cases markedly, from that obtained from phenomenological or real-interaction shell models.

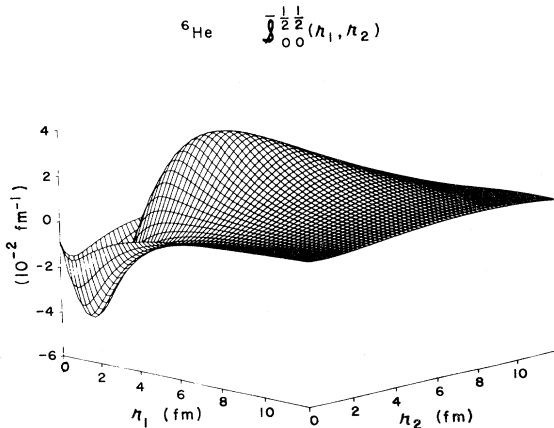


FIG. 19.  ${}^6\text{He}$  full  $(np)$  model  $(s_{1/2})^2$  two-body configuration-space reduced wave-function amplitude,  $\mathcal{S} = r_1 r_2 \mathcal{S}$ .

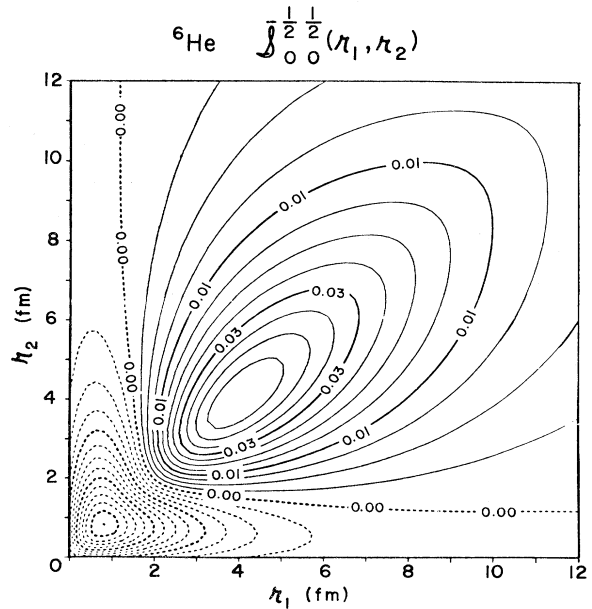


FIG. 20. Contour plot of amplitude given in Fig. 19.

In the future, these aspects can be explored at a deeper level to determine the effect of these differences in one-body transition densities, the key elements in all transitions involving a single nucleon. The present work suggests that the differences will be significant.

Besides the fact that three-body models of the  $A=6$  system involve proper three-body dynamics once the basic  $\alpha N$  and  $NN$  interactions are specified, they also have the advantage of being set up and solved in the center-of-mass system. This is particularly important for light nuclei such as  ${}^6\text{He}$  and  ${}^6\text{Li}$ . Nevertheless, for one accustomed to dealing with oscillator shell models of  ${}^6\text{He}$  and  ${}^6\text{Li}$ , the details of the present calculation may appear quite involved. Part of the complication comes about because of the transformation to the coordinates of the nucleons relative to the alpha particle from the center-of-mass Jacobi coordinates. The other part comes from the three-body dynamics, an ingredient which, in our opinion, can no longer be ignored in our quest to better understand the  $A=6$  system. Specifically, along this line, our principal findings are the following:

(1) The three-body values of the  $A=6$  shell-orbital probabilities echo the nature of the underlying  $\alpha N$  interactions. The  $p_{3/2}$  orbital dominates because of the strongly resonant  $P_{3/2}$  wave of the  $\alpha N$  interaction, whereas the  $s_{1/2}$  orbital is suppressed due to the Pauli principle manifest through the repulsive  $S_{1/2}$  wave of the  $\alpha N$  interaction.

(2) None of the oscillator shell models considered, phenomenological or realistic interaction, have a distribution of orbital probabilities in the  $p$  shell like that predicted by our three-body models. Allowing for core excitation in realistic-interaction shell

models tends to move the shell-model results towards the three-body values, but this serves to emphasize that an *apparent* need for core excitation may actually indicate a need to move from "effective" two-body dynamics to three-body dynamics.

(3) The location of the maxima of the single-particle orbital densities from the three-body models order the orbits within shells, i.e., the maxima of the  $(p_{1/2})^2$  orbital occurs at a distance  $\sim 0.8$  fm beyond that for the  $(p_{3/2})^2$  orbital, etc. These shell properties are further supported by the calculated rms orbital radii (Table VI). In oscillator shell models with a single oscillator parameter, the maxima of the  $(p_{3/2})^2$  and  $(p_{1/2})^2$  orbitals occur at the same radial distance, etc.

(4) Three-body models give physically sensible exponentially decaying single-particle orbital densities at large radial distances compared to the unrealistic, compact, Gaussian shape of oscillator shell models.

These findings lead us to believe that calculation of the  $A=6$  system low-excitation properties and processes with three-body models will give a far more realistic and *complete* description than that obtained from shell models.

#### ACKNOWLEDGMENTS

The authors would like to thank T. W. Donnelly for several discussions concerning this work and for calculating the Woods-Saxon wave function appearing in Fig. 16. Also, the authors are grateful to Dr. Donald Orser and Mr. Stuart Kramer for generating the three-dimensional graphs and contour plots. The work of D. R. L. was supported in part by the Department of Energy.

#### APPENDIX A

In this appendix, we give the  ${}^6\text{He}$  and  ${}^6\text{Li}$  wave functions expanded into shell angular states and expressed in terms of the three-body spectator functions and two body form factors defined in Sec. II.

For  ${}^6\text{He}(0^+)$ ,

$$\Psi^{[0]}(\vec{\mu}_1, \vec{\mu}_2) = \sum_{JL} \mathcal{F}_L^J(\mu_1, \mu_2) [\mathcal{Y}_{L(1/2)}^{[J]}(\hat{\mu}_1, 1) \times \mathcal{Y}_{L(1/2)}^{[J]}(\hat{\mu}_2, 2)]^{[0]}, \quad (\text{A1})$$

where

$$\begin{aligned} \mathcal{F}_L^J(\mu_1, \mu_2) = & (-1)^{L+J} 4\sqrt{2} \hat{J} \int_0^\infty \int_0^\infty p_1^2 dp_1 p_2^2 dp_2 [j_L(\mu_1 p_1) j_L(\mu_2 p_2) + j_L(\mu_2 p_1) j_L(\mu_1 p_2)] \\ & \times \left[ \frac{1}{2} \mathcal{G}_L(p_1, p_2) - \mathcal{F}_{0L}(p_1, p_2) + p_1 \mathcal{F}_{1(2J-L)}(p_1, p_2) + \frac{1}{5} p_2 \mathcal{F}_{1L}(p_1, p_2) \right. \\ & + \frac{3}{\sqrt{2}} \frac{(2J+2-L)}{2L+1} p_1 \mathcal{F}_{3(2J+2-L)}(p_1, p_2) \\ & \left. + \frac{1}{\sqrt{2}} \frac{(3J-2L+\frac{1}{2})}{2L+1} p_1 \mathcal{F}_{3(2J-L)}(p_1, p_2) + \frac{\sqrt{2}}{5} p_2 \mathcal{F}_{3L}(p_1, p_2) \right], \quad (\text{A2}) \end{aligned}$$

$$\mathcal{G}_L(p_1, p_2) = \frac{\lambda_0}{2} \int_{-1}^1 d\xi P_L(\xi) \frac{g_0^0[\frac{1}{2}(p_1^2 + p_2^2 - 2p_1 p_2 \xi)^{1/2}] G^0[(p_1^2 + p_2^2 + 2p_1 p_2 \xi)^{1/2}]}{K_{\text{He}}^2 + \frac{5}{8}(p_1^2 + p_2^2) + \frac{1}{4}p_1 p_2 \xi}, \quad (\text{A3})$$

$$\mathcal{F}_{(2j+l-1)}(p_1, p_2) = \frac{5\Lambda_l^j}{16} \int_{-1}^1 d\xi P_L(\xi) \frac{\mathcal{H}_l^j[(p_1^2 + \frac{1}{25}p_2^2 + \frac{2}{5}p_1 p_2 \xi)^{1/2}] F_l^j(p_2)}{K_{\text{He}}^2 + \frac{5}{8}(p_1^2 + p_2^2) + \frac{1}{4}p_1 p_2 \xi}, \quad (\text{A4})$$

and

$$\mathcal{H}_l^j(k) = h_l^j(k)/k^l. \quad (\text{A5})$$

The  $1^+$  state of  ${}^6\text{Li}$  is described by the following wave function:

$$\Psi_M^{[1]}(\vec{\kappa}_1, \vec{\kappa}_2) = \sum \mathcal{S}_{L_1 L_2}^{J_1 J_2}(\kappa_1, \kappa_2) [\mathcal{Y}_{L_1(1/2)}^{[J_1]}(\hat{\kappa}_1, 1) \times \mathcal{Y}_{L_2(1/2)}^{[J_2]}(\hat{\kappa}_2, 2)]_M^{[1]} \quad (\text{A6})$$

with

$$\begin{aligned} \mathcal{S}_{L_1 L_2}^{J_1 J_2}(\kappa_1, \kappa_2) &= (-1)^{(L_1 + L_2)/2} 4 \int \int dp_1 dp_2 p_1^2 p_2^2 j_{L_1}(p_1 \kappa_1) j_{L_2}(p_2 \kappa_2) \\ &\times \int_{-1}^1 d\xi \frac{\sum_{l, l'=0,2} \left[ \overline{\mathcal{G}}_{L_1 L_2 l l'}^{J_1 J_2} + \sum_{JJ'} \overline{\mathcal{F}}_{L_1 L_2 l l'}^{J_1 J_2 JJ'} \right]}{K_{\text{Li}}^2 + \frac{5}{8}(p_1^2 + p_2^2) + \frac{1}{4}p_1 p_2 \xi}, \end{aligned} \quad (\text{A7})$$

where

$$\overline{\mathcal{G}}_{L_1 L_2 00}^{J_1 J_2} = \mathcal{G}_{00} \delta_{L_1 L_2} \hat{J}_1 \hat{J}_2 \hat{1} \hat{L}_1 \begin{bmatrix} J_1 & J_2 & 1 \\ L_1 & L_2 & 0 \\ \frac{1}{2} & \frac{1}{2} & 1 \end{bmatrix} P_{L_1}(\xi), \quad (\text{A8})$$

$$\begin{aligned} \overline{\mathcal{F}}_{LL 20}^{J_1 J_2} &= \mathcal{G}_{20}^{02} \hat{J}_1 \hat{J}_2 \hat{1} \hat{L} \hat{2} \left[ \frac{L(L+1)}{(2L+3)(2L-1)} \right]^{1/2} \begin{bmatrix} J_1 & J_2 & 1 \\ L & L & 2 \\ \frac{1}{2} & \frac{1}{2} & 1 \end{bmatrix} \\ &\times \left[ \frac{(p_1^2 + p_2^2)P_L \pm \frac{p_1 p_2}{2L+1} [(2L-1)P_{L+1} + (2L+3)P_{L-1}]}{p_1^2 + p_2^2 \pm 2p_1 p_2 \xi} \right], \end{aligned} \quad (\text{A9})$$

$$\overline{\mathcal{F}}_{L(L+2) 20}^{J_1 J_2} = \mathcal{G}_{20}^{02} \hat{J}_1 \hat{J}_2 \hat{3} \left[ \frac{2 \times 5(L+1)(L+2)}{(2L+3)} \right]^{1/2} \begin{bmatrix} J_1 & J_2 & 1 \\ L & L+2 & 2 \\ \frac{1}{2} & \frac{1}{2} & 1 \end{bmatrix} \left[ \frac{p_1^2 P_{L+2} + p_2^2 P_L \pm 2p_1 p_2 P_{L+1}}{p_1^2 + p_2^2 \pm 2p_1 p_2 \xi} \right], \quad (\text{A10})$$

$$\begin{aligned}
 \overline{\mathcal{F}}_{LL22}^{J_1 J_2} = & \mathcal{G}_{22} \left[ \hat{J}_1 \hat{J}_2 \hat{1} \hat{L} \begin{bmatrix} J_1 & J_2 & 1 \\ L & L & 0 \\ \frac{1}{2} & \frac{1}{2} & 1 \end{bmatrix} \left[ \frac{p_1^4 + p_2^4 - 4p_1^2 p_2^2 + 2p_1^2 p_2^2 \xi^2}{p_1^4 + p_2^4 - 4p_1^2 p_2^2 \xi^2 + 2p_1^2 p_2^2} \right] P_L \right. \\
 & + \hat{J}_1 \hat{J}_2 \frac{9}{2} \left[ \frac{3L(L+1)}{2(2L+1)} \right]^{1/2} \begin{bmatrix} J_1 & J_2 & 1 \\ L & L & 1 \\ \frac{1}{2} & \frac{1}{2} & 1 \end{bmatrix} \left[ \frac{2p_1 p_2 (p_1^2 - p_2^2)}{p_1^4 + p_2^4 - 4p_1^2 p_2^2 \xi^2 + 2p_1^2 p_2^2} \right] (P_{L-1} - P_{L+1}) \\
 & + \hat{J}_1 \hat{J}_2 \left[ \frac{3 \times 5L(L+1)(2L+1)}{2(2L+3)(2L-1)} \right]^{1/2} \begin{bmatrix} J_1 & J_2 & 1 \\ L & L & 2 \\ \frac{1}{2} & \frac{1}{2} & 1 \end{bmatrix} \\
 & \left. \times \left[ \frac{(p_1^4 + p_2^4 - 10p_1^2 p_2^2) P_L + \frac{4p_1^2 p_2^2 \xi}{2L+1} [(2L-1)P_{L+1} + (2L+3)P_{L-1}]}{p_1^4 + p_2^4 - 4p_1^2 p_2^2 \xi^2 + 2p_1^2 p_2^2} \right] \right], \tag{A11}
 \end{aligned}$$

$$\begin{aligned}
 \overline{\mathcal{F}}_{L(L+2)22}^{J_1 J_2} = & \mathcal{G}_{22} \hat{J}_1 \hat{J}_2 3 \left[ \frac{5(L+1)(L+2)}{(2L+3)} \right]^{1/2} \begin{bmatrix} J_1 & J_2 & 1 \\ L & L+2 & 2 \\ \frac{1}{2} & \frac{1}{2} & 1 \end{bmatrix} \\
 & \times \left[ \frac{(p_1^2 - 5p_2^2)p_1^2 P_{L+2} + (p_2^2 - 5p_1^2)p_2^2 P_L + 8p_1^2 p_2^2 \xi^2 P_{L+1}}{p_1^4 + p_2^4 - 4p_1^2 p_2^2 \xi^2 + 2p_1^2 p_2^2} \right], \tag{A12}
 \end{aligned}$$

$$\overline{\mathcal{F}}_{L_1 L_2 l l'}^{J_1 J_2 J J'} = (-1)^{l+J_2+J'+1} \sum_{L=L_1 \pm l} \left[ \begin{bmatrix} J_1 & J_2 & J & J' & 1 \\ L_1 & L_2 & l & l' & L \end{bmatrix} f_{LL_1}^l(p_1, p_2, \xi) + \begin{bmatrix} J_2 & J_1 & J & J' & 1 \\ L_2 & L_1 & l & l' & L \end{bmatrix} f_{LL_2}^l(p_2, p_1, \xi) \right], \tag{A13}$$

$$\begin{aligned}
 \begin{bmatrix} J_1 & J_2 & J & J' & 1 \\ L_1 & L_2 & l & l' & L \end{bmatrix} & \equiv \hat{J}_1 \hat{J}_2 \hat{L}_1 \hat{L}_2 \hat{J} \hat{J}' \hat{1} \hat{1}' (-1)^L \hat{L}^2 \begin{bmatrix} l & L_1 & L \\ J_1 & J & \frac{1}{2} \end{bmatrix} \begin{bmatrix} l' & L_2 & L \\ J_2 & J' & \frac{1}{2} \end{bmatrix} \\
 & \times \begin{bmatrix} J_1 & J_2 & 1 \\ J' & J & L \end{bmatrix} \left| \begin{bmatrix} l & L_1 & L \\ 0 & 0 & 0 \end{bmatrix} \begin{bmatrix} l' & L_2 & L \\ 0 & 0 & 0 \end{bmatrix} \right|, \tag{A14}
 \end{aligned}$$

$$f_{LL_1}^0(p_1, p_2, \xi) \equiv \mathcal{F}_{0l'}^{(1/2)J'}(k_{31}, p_2) P_{L_1}(\xi), \tag{A15}$$

$$f_{LL_1}^1(p_1, p_2, \xi) \equiv \mathcal{F}_{ll'}^{JJ'}(k_{31}, p_2) \left[ \frac{p_1}{k_{31}} P_L(\xi) + \frac{p_2}{5k_{31}} P_{L_1}(\xi) \right], \tag{A16}$$

$$\mathcal{G}_{ll'}(k_{12}, p_3) \equiv \lambda_1 g_l^1(k_{12}) G^{l'}(p_3), \tag{A17}$$

and

$$\mathcal{F}_{ll'}^{JJ'}(k_{31}, p_2) \equiv \frac{5}{8} \Lambda_l^J h_l^J(k_{31}) F_{l'(J)}^{J'}(p_2). \tag{A18}$$

## APPENDIX B

The purpose of this appendix is to illustrate in a simple manner that if the two-particle wave function amplitude,  $\mathcal{S}_{00}^{(1/2)(1/2)}(\kappa_1, \kappa_2)$  in Fig. 19, has a node, then the single-particle orbital density,  $P_{00}^{(1/2)(1/2)}(\kappa_1)$  in Fig. 7, will have a minimum for  $\kappa_1 \neq 0$ .

We set up a simple analytical model using a product of oscillator wave functions. The relative motion of the two nucleons is taken as  $1s$  while the relative motion of the alpha particle with respect to the two-nucleon center of mass is  $2s$  (Ref. 6):

$$\begin{aligned} \Psi(\vec{r}, \vec{p}) &\equiv \Psi(\vec{\kappa}_1, \vec{\kappa}_2) \\ &= \left[ \frac{3}{2} \right]^{1/2} \left[ \frac{2\nu}{\pi} \frac{2\nu'}{\pi} \right]^{3/4} \exp \left[ -\nu(\kappa_1^2 + \kappa_2^2 - 2\vec{\kappa}_1 \cdot \vec{\kappa}_2) - \frac{\nu'}{4}(\kappa_1^2 + \kappa_2^2 + 2\vec{\kappa}_1 \cdot \vec{\kappa}_2) \right] \\ &\quad \times \left[ 1 - \frac{\nu'}{3}(\kappa_1^2 + \kappa_2^2 + 2\vec{\kappa}_1 \cdot \vec{\kappa}_2)^2 \right], \end{aligned} \quad (\text{B1})$$

where for the  $A=6$  system  $\nu \sim 2\nu'$ . Clearly, this form leads to an  $\mathcal{S}(\kappa_1, \kappa_2)$  with nodal behavior like  $\mathcal{S}_{00}^{(1/2)(1/2)}(\kappa_1, \kappa_2)$ . Then, we calculate analytically

$$\begin{aligned} P(\kappa_1) &= \kappa_1^2 \int d\Omega_1 d^3\kappa_2 \Psi^*(\vec{\kappa}_1, \vec{\kappa}_2) \Psi(\vec{\kappa}_1, \vec{\kappa}_2), \\ &= 2 \left[ \frac{2\nu^3(4\nu + \nu')}{\nu} \right]^{1/2} y^2 \exp \left[ -\frac{\nu'(4\nu + \nu')}{8\nu} y^2 \right] \left[ \frac{2}{3} \frac{\nu'^2 + 24\nu^2}{(4\nu + \nu')^2} + \frac{4\nu'}{9} \frac{\nu' - 6\nu}{4\nu + \nu'} y^2 + \frac{\nu'^2}{9} y^4 \right], \end{aligned} \quad (\text{B2})$$

$$(\text{B3})$$

where  $y = 8\nu\kappa_1/(4\nu + \nu')$ . Independent of the relative sizes of  $\nu$  and  $\nu'$ , the quantity in the brackets is never zero for *real*  $y$ . Therefore, the node that was present in Eq. (B1) has disappeared in  $P(\kappa_1)$ . Furthermore, Eq. (B3) has two maxima and a minima between 0 and  $\infty$  for the realistic relationship  $\nu \sim 2\nu'$ , but not for  $\nu \sim \nu'$ . Thus, when  $\nu \sim 2\nu'$ , a graph like Fig. 7 results.

These simple considerations have their origins in a more general theorem that can be proved concerning the nodal structure of single-particle orbital densities as it relates to the underlying two-particle, wave-function amplitudes.

<sup>1</sup>Y. Koike, Prog. Theor. Phys. **59**, 87 (1978); Nucl. Phys. **A301**, 411 (1978); **A337**, 23 (1980). See also the earlier work of P. E. Shanley, Phys. Rev. **187**, 1328 (1969); B. Charnomordic, C. Fayard, and G. H. Lamot, Phys. Rev. C **15**, 864 (1977).

<sup>2</sup>Y. Matsui, Phys. Rev. C **22**, 2591 (1980).

<sup>3</sup>A. Ghovanlou and D. R. Lehman, Phys. Rev. C **9**, 1730 (1974).

<sup>4</sup>D. R. Lehman, M. Rai, and A. Ghovanlou, Phys. Rev. C **17**, 744 (1978).

<sup>5</sup>D. R. Lehman, Phys. Rev. C **25**, 3146 (1982).

<sup>6</sup>D. R. Lehman and Mamta Rajan, Phys. Rev. C **25**, 2743 (1982). See also the earlier work of M. Rai, D. R. Lehman, and A. Ghovanlou, Phys. Lett. **59B**, 327 (1975).

<sup>7</sup>W. C. Parke, A. Ghovanlou, C. T. Noguchi, M. Rajan, and D. R. Lehman, Phys. Lett. **74B**, 158 (1978).

<sup>8</sup>See J. Bang and C. Gignoux, Nucl. Phys. **A313**, 119 (1979), for a first calculation of the charge radius and charge form factor of  ${}^6\text{Li}$  with a three-body model

somewhat less complete than those used in the work described above. Also, V. T. Voronchev, V. M. Krasnopol'sky, V. I. Kukulín, and P. B. Sazonov, J. Phys. G **8**, 667 (1982), where a variational three-body wave function is used.

<sup>9</sup>As an example, see A. Dellafiore and M. Traini, Nucl. Phys. **A344**, 509 (1980).

<sup>10</sup>T. W. Donnelly and J. D. Walecka, Phys. Lett. **44B**, 330 (1973).

<sup>11</sup>J. F. Dawson and J. D. Walecka, Ann. Phys. (N.Y.) **22**, 133 (1963).

<sup>12</sup>J. C. Bergstrom, I. P. Auer, and R. S. Hicks, Nucl. Phys. **A251**, 401 (1975).

<sup>13</sup>J. B. Cammarata and T. W. Donnelly, Nucl. Phys. **A267**, 365 (1976).

<sup>14</sup>G. Audit, A. Bloch, N. deBotton, C. Schuhl, G. Tamas, C. Tzara, J. Deutsch, D. Favart, R. Prieels, and B. Van Oystaeyen, Phys. Rev. C **15**, 1415 (1977).

<sup>15</sup>J. D. Vergados, Nucl. Phys. **A220**, 259 (1974).

- <sup>16</sup>T. T. S. Kuo and G. E. Brown, Nucl. Phys. 85, 40 (1966); A92, 481 (1967).
- <sup>17</sup>D. R. Lehman and W. C. Parke, Phys. Rev. Lett. 50, 98 (1983).
- <sup>18</sup>The notation follows that in Refs. 3 and 4. For example,  $Y_m^{l1}(\hat{k}) = (-i)^l Y_{lm}(\hat{k})$  and  $\chi_m^{[1/2]} = \chi_{(1/2)m}$ .
- <sup>19</sup>M. Danos, Ann. Phys. (N.Y.) 63, 319 (1971).
- <sup>20</sup>D. R. Lehman, W. C. Parke, and L. C. Maximon, J. Math. Phys. 22, 1399 (1981).
- <sup>21</sup>In very-large-basis shell-model calculations, where an attempt is made to accurately reproduce the  ${}^6\text{Li}$  states, the  $s$ - $d$  shell is found to play a significant role. See the work of J. M. Irvine, G. S. Mani, V. F. E. Pucknell, M. Vallieres, and F. Yazici, Ann. Phys. (N.Y.) 102, 129 (1976); R. Ceuleneer, M. Erculisse, and M. Gilles, Phys. Lett. 65B, 101 (1976).
- <sup>22</sup>For the Donnelly-Walecka oscillator parameter (see Table I), the  $1p$ -shell rms orbital radii are identical and equal to 4.30 fm. Using the same parameter for the  $s$ - $d$  shell yields 4.76 fm for the orbital radii.
- <sup>23</sup>This aspect of the Woods-Saxon models stands out in another way—in the choice of the  $p_{3/2}$  and  $p_{1/2}$  separation energies, i.e., in the strength of the spin-orbit interaction. Typical values would be 3.84 and 1.00 MeV for the  $p_{3/2}$  and  $p_{1/2}$  separation energies, respectively (Ref. 13). To an accuracy of approximately 10%, the exponential falloff of the three-body single-particle densities yields for the separation energies values that indicate a much weaker effective spin-orbit-interaction strength than is usually assumed. Specifically, for  ${}^6\text{He}(nn)$ :  $p_{3/2} - 0.95$  MeV and  $p_{1/2} - 0.85$  MeV; while for  ${}^6\text{Li}$  (4%):  $p_{3/2}(p_{3/2}) - 3.45$  MeV,  $p_{3/2}(p_{1/2}) - 3.32$  MeV,  $p_{1/2}(p_{3/2}) - 3.26$  MeV, and  $p_{1/2}(p_{1/2}) - 3.02$  MeV. The three-body separation energies reflect in their absolute magnitude the size of the total three-body binding energy and they are consistent with the computed rms orbital radii.
- <sup>24</sup>T. W. Donnelly, private communication. See T. W. Donnelly and W. C. Haxton, At. Data Nucl. Data Tables 23, 103 (1979).